Chapter 8

TELEPORTATION SYSTEMS TOWARDS A QUANTUM INTERNET

This chapter includes the work published as:

[1] Raju Valivarthi, Samantha I. Davis, Cristián Peña, Si Xie, Nikolai Lauk, Lautaro Narváez, Jason P. Allmaras, Andrew D. Beyer, Yewon Gim, Meraj Hussein, et al. "Teleportation systems toward a quantum internet." In: PRX Quantum 1.2 (2020), p. 020317.

8.1 Introduction

Quantum teleportation [1], one of the most captivating predictions of quantum theory, has been widely investigated since its seminal demonstrations over 20 years ago [2, 3, 4]. This is due to its connections to fundamental physics [5, 6, 7, 8, 9, 10, 11, 12, 13, 14], and its central role in the realization of quantum information technology such as quantum computers and networks [15, 16, 17, 18, 19]. The goal of a quantum network is to distribute qubits between different locations, a key task for quantum cryptography, distributed quantum computing and sensing. A quantum network is expected to form part of a future quantum internet [20, 21, 22]: a globally distributed set of quantum processors, sensors, or users there-of that are mutually connected over a network capable of allocating quantum resources (e.g., qubits and entangled states) between locations. Many architectures for quantum networks require quantum teleportation, such as star-type networks that distribute entanglement from a central location or quantum repeaters that overcome the rate-loss trade-off of direct transmission of qubits [19, 23, 24, 25, 26].

Quantum teleportation of a qubit can be achieved by performing a Bell-state measurement (BSM) between the qubit and another that forms one member of an entangled Bell state [1, 18, 27]. The quality of the teleportation is often characterized by the fidelity $F = \langle\psi|\,\rho\,|\psi\rangle$ of the teleported state ρ with respect to the state $|\psi\rangle$ accomplished by ideal generation and teleportation [15]. This metric is becoming increasingly important as quantum networks move beyond specific applications, such as quantum key distribution, and towards the quantum internet.

Qubits encoded by the time-of-arrival of individual photons, i.e., time-bin qubits [28], are useful for networks due to their simplicity of generation, interfacing with quantum devices, as well as independence of dynamic transformations of real-world fibers. Individual telecom-band photons (around 1.5 μm wavelength) are ideal carriers of qubits in networks due to their ability to rapidly travel over long distances in deployed optical fibers [17, 29, 30, 31] or atmospheric channels [32], among other properties. Moreover, the improvement and growing availability of sources and detectors of individual telecom-band photons has accelerated progress towards workable quantum networks and associated technologies, such as quantum memories [33], transducers [34, 35], or quantum non-destructive measurement devices [36].

Teleportation of telecom-band photonic time-bin qubits has been performed inside and outside the laboratory with impressive results [37, 38, 39, 40, 41, 30, 29, 42, 31]. Despite this, there has been little work to increase F beyond $\sim 90\%$ for these qubits, in particular using practical devices that allow straightforward replication and deployment of quantum networks (e.g., using fiber-coupled and commercially available devices). Moreover, it is desirable to develop teleportation systems that are forward-compatible with emerging quantum devices for the quantum internet.

In the context of Caltech's multi-disciplinary multi-institutional collaborative public-private research program on Intelligent Quantum Networks and Technologies (IN-Q-NET) founded with AT&T as well as Fermi National Accelerator Laboratory (Fermilab) and Jet Propulsion Laboratory in 2017, we designed, built, commissioned and deployed two quantum teleportation systems: one at Fermilab, the Fermilab Quantum Network (FQNET), and one at Caltech's Lauritsen Laboratory for High Energy Physics, the Caltech Quantum Network (CQNET). The CQNET system serves as an R&D, prototyping, and commissioning system, while FQNET serves as an expandable system, for scaling up to long distances and is used in multiple projects funded currently by DOE's Office of High Energy Physics (HEP) and Advanced Scientific Research Computing (ASCR). Material and devices level R&D in both systems is facilitated and funded by the Office of Basic Energy Sciences. Both systems are accessible to quantum researchers for R&D purposes as well as testing and integration of various novel devices, such as for example on-chip integrated nanophotonic devices and quantum memories, needed to upgrade such systems towards a realistic quantum internet. Importantly both systems are also used for improvements of the entanglement quality and distribution with emphasis on implementation of protocols with complex entangled states towards advanced and complex quantum communications channels. These will assist in studies of systems that implement new teleportation protocols whose gravitational duals correspond to wormholes [43], error correlation properties of wormhole teleportation, on-chip codes as well as possible implementation of protocols on quantum optics communication platforms. Hence the systems serve both fundamental quantum information science as well as quantum technologies.

Here we perform quantum teleportation of time-bin qubits at a wavelength of 1536.5 nm with an average $F \geq 90\%$. This is accomplished using a compact setup of fiber-coupled devices, including low-dark-count single photon detectors and off-the-shelf optics, allowing straight-forward reproduction for multi-node networks. To illustrate network compatibility, teleportation is performed with up to 44 km of single-mode fiber between the qubit generation and the measurement of the teleported qubit, and is facilitated using semi-autonomous control, monitoring, and synchronization systems, with results collected using scalable acquisition hardware. Our systems, which operates at a clock rate of 90 MHz, can be run remotely for several days without interruption and yield teleportation rates of a few Hz using the full length of fiber. Our qubits are also compatible with erbium-doped crystals, e.g., Er:Y_2SiO_5, that are used to develop quantum network devices like memories and transducers [44, 45, 46]. Finally, we develop an analytical model of our system, which includes experimental imperfections, predicting that the fidelity can be improved further towards unity by well-understood methods (such as improvement in photon indistinguishability). Our demonstrations provide a step towards a workable quantum network with practical and replicable nodes, such as the ambitious U.S. Department of Energy quantum research network envisioned to link the U.S. National Laboratories.

In the following we describe the components of our systems as well as characterization measurements that support our teleportation results, including the fidelity of our entangled Bell state and Hong-Ou-Mandel (HOM) interference [47] that underpins the success of the BSM. We then present our teleportation results using both quantum state tomography (QST) [48] and projection measurements based on a decoy state method [49], followed by a discussion of our model. We conclude by considering improvements towards near-unit fidelity and GHz level teleportation rates.

8.2 Setup

Our fiber-based experimental system is summarized in the diagram of Fig. 8.1. It allow us to demonstrate a quantum teleportation protocol in which a photonic qubit (provided by Alice) is interfered with one member of an entangled photon-pair (from Bob) and projected (by Charlie) onto a Bell-state whereby the state of Alice's qubit can be transferred to the remaining member of Bob's entangled photon pair. Up to 22 (11) km of single mode fiber is introduced between Alice and Charlie (Bob and Charlie), as well as up to another 11 km at Bob, depending on the experiment (see Sec. 8.3). All qubits are generated at the clock rate, with all of their measurements collected using a data acquisition (DAQ) system. Each of the Alice, Bob, Charlie subsystems are further detailed in the following subsections, with the DAQ subsystem described in Section 8.6.

Alice: single-qubit generation

To generate the time-bin qubit that Alice will teleport to Bob, light from a fiber-coupled 1536.5 nm continuous wave (CW) laser is input into a lithium niobate intensity modulator (IM). We drive the IM with one pulse, or two pulses separated by 2 ns. Each pulse is of ~65 ps full width at half maximum (FWHM) duration. The pulses are produced by an arbitrary waveform generator (AWG) and amplified by a 27 dB-gain high-bandwidth amplifier to generate optical pulses that have an extinction ratio of up to 22 dB. We note that this method of creating time-bin qubits offers us flexibility not only in terms of choosing a suitable time-bin separation, but also for synchronizing qubits originating from different nodes in a network. A 90/10 polarization-maintaining fiber beam splitter combined with a power monitor (PWM) is used to apply feedback to the DC-bias port of the IM so as to maintain a constant 22 dB extinction ratio [50]. In order to successfully execute the quantum teleportation protocol, photons from Alice and Bob must be indistinguishable in all degrees of freedom (see Sec. 8.3). Hence, the optical pulses at the output of the IM are band-pass filtered using a 2 GHz-bandwidth (FWHM) fiber Bragg grating (FBG) centered at 1536.5 nm to match the spectrum of the photons from the entangled pair-source (described in Sec. 8.2). Furthermore, the polarization of Alice's photons is determined by a manual polarization controller (POC) in conjunction with a polarizing beam splitter (PBS) at Charlie. Finally, the optical pulses from Alice are attenuated to the single photon level by a variable optical attenuator (VOA), to approximate photonic time-bin qubits of the form $|A\rangle = \gamma\,|e\rangle_A + \sqrt{1-\gamma^2}\,|l\rangle_A$, where the late state $|l\rangle_A$ arrives 2 ns after the early state $|e\rangle_A$, γ is real and set to be

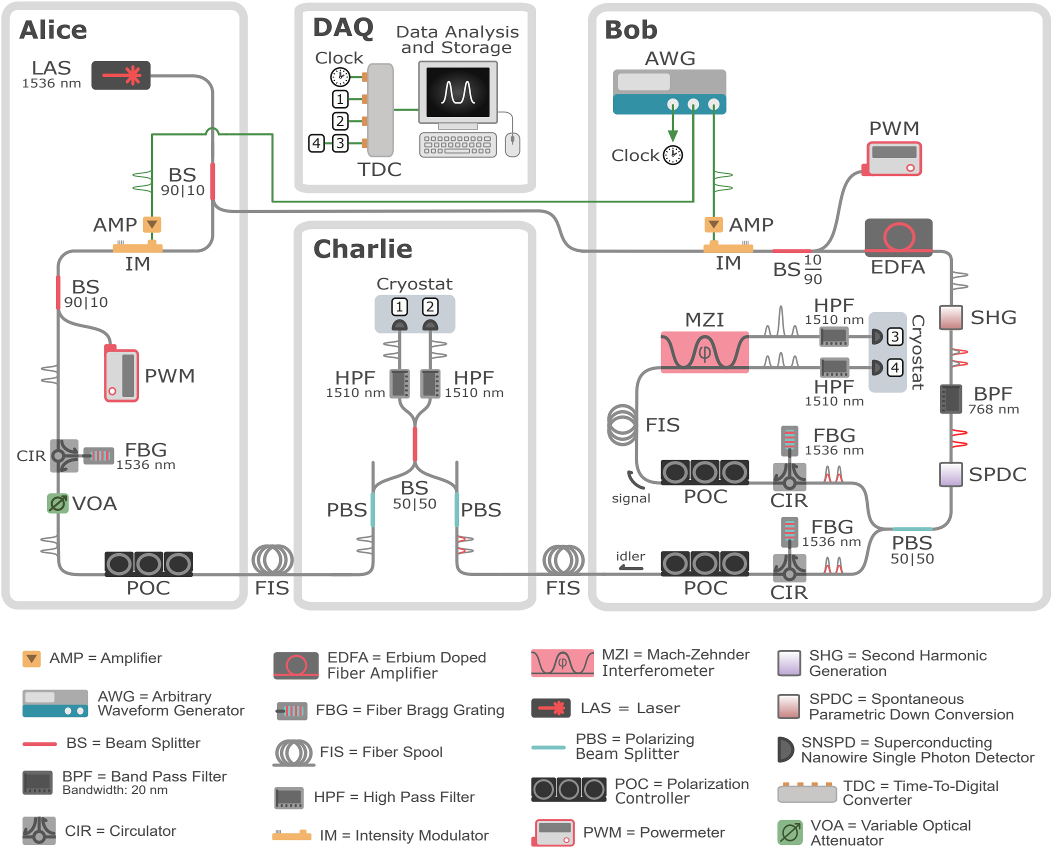
Alice
LAS
1536 nm
BS
90|10
AMP
IM
BS
90|10
PWM
CIR
FBG
1536 nm
VOA
POC
FIS
DAQ
Data Analysis
and Storage
Clock
1
2
3
4
TDC
Charlie
Cryostat
1
2
HPF
1510 nm
HPF
1510 nm
BS
50|50
PBS
PBS
FIS
Bob
AWG
Clock
PWM
AMP
IM
BS
10
90
EDFA
MZI
φ
HPF
1510 nm
HPF
1510 nm
3
4
Cryostat
SHG
BPF
768 nm
FIS
FBG
1536 nm
signal
POC
CIR
SPDC
FBG
1536 nm
idler
POC
CIR
PBS
50|50
AMP = Amplifier
AWG = Arbitrary Waveform Generator
BS = Beam Splitter
BPF = Band Pass Filter
Bandwidth: 20 nm
CIR = Circulator
EDFA = Erbium Doped Fiber Amplifier
FBG = Fiber Bragg Grating
FIS = Fiber Spool
HPF = High Pass Filter
IM = Intensity Modulator
MZI = Mach-Zehnder Interferometer
LAS = Laser
PBS = Polarizing Beam Splitter
POC = Polarization Controller
PWM = Powermeter
SHG = Second Harmonic Generation
SPDC = Spontaneous Parametric Down Conversion
SNSPD = Superconducting Nanowire Single Photon Detector
TDC = Time-To-Digital Converter
VOA = Variable Optical Attenuator

Figure 8.1: Schematic diagram of the quantum teleportation system consisting of Alice, Bob, Charlie, and the data acquisition (DAQ) subsystems. See the main text for descriptions of each subsystem. One cryostat is used to house all SNSPDs, it is drawn as two for ease of explanation. Detection signals generated by each of the SNSPDs are labelled 1-4 and collected at the TDC, with 3 and 4 being time-multiplexed. All individual components are labeled in the legend, with single-mode optical fibers (electronic cables) in grey (green), and with uni- and bi-chromatic (i.e., unfiltered) optical pulses indicated.

either 1, 0, or $1/\sqrt{2}$ to generate $|e\rangle_A$, $|l\rangle_A$, or $|+\rangle_A = (|e\rangle_A + |l\rangle_A)/\sqrt{2}$, respectively, depending on the experiment. The complex relative phase is absorbed into the definition of $|l\rangle_A$. The duration of each time bin is 800 ps.

Bob: entangled qubit generation and teleported-qubit measurement

Similar to Alice, one (two) optical pulse(s) with a FWHM of $\sim$ 65 ps is (and separated by 2 ns are) created using a 1536.5 nm CW laser in conjunction with a lithium niobate IM driven by an AWG, while the 90/10 beam splitter and PWM are used to maintain an extinction ratio of at least 20 dB. An Erbium-Doped Fiber Amplifier (EDFA) is used after the IM to boost the pulse power and thus maintain a high output rate of photon pairs.

The output of the EDFA is sent to a Type-0 periodically poled lithium niobate (PPLN) waveguide for second harmonic generation (SHG), upconverting the pulses to 768.25 nm. The residual light at 1536.5 nm is removed by a 768 nm bandpass filter with an extinction ratio $\geq$ 80 dB. These pulses undergo spontaneous parametric down-conversion (SPDC) using a Type-II PPLN waveguide coupled to a polarization-maintaining fiber (PMF), approximately producing either a photon pair $|pair\rangle_B = |ee\rangle_B$, or the time-bin entangled state $|\phi^+\rangle_B = (|ee\rangle_B + |ll\rangle_B)/\sqrt{2}$, if one or two pulses, respectively, are used to drive the IM. The ordering of the states refers to so-called signal and idler modes of the pair of which the former has parallel, and the latter orthogonal, polarization with respect to the axis of the PMF. As before, the relative phase is absorbed into the definition of $|ll\rangle_B$. Each photon is separated into different fibers using a PBS and spectrally filtered with FBGs akin to that at Alice. Note the bandwidth of the FBG is chosen as a trade-off between spectral purity and generation rate of Bob's photons [51]. The photon in the idler mode is sent to Charlie for teleportation or HOM measurements (see Sec. 8.3), or to the MZI (see below) for characterizations of the entangled state (see Sec. 8.3), with its polarization determined using a POC. The photon in the signal mode is sent to a Mach Zehnder interferometer (MZI) by way of a POC (and an additional 11 km of single-mode fiber for some measurements), and is detected by superconducting nanowire single photon detectors (SNSPDs) [52] after high-pass filtering (HPF) to reject any remaining 768.25 nm light. The MZI and detectors are used for projection measurements of the teleported state, characterization of the time-bin entangled state, or measuring HOM interference at Charlie. The time-of-arrival of the photons is recorded by the DAQ subsystem using a time-to-digital converter (TDC) referenced to the clock signal from the AWG.

All SNSPDs are installed in a compact sorption fridge cryostat [53], which operates at a temperature of 0.8 K for typically 24 h before a required 2 h downtime. Our SNSPDs are developed at the Jet Propulsion Laboratory and have detection efficiencies between 76 and 85%, with low dark count rates of 2-3 Hz. The FWHM temporal resolution of all detectors is between 60 and 90 ps while their recovery time is ~50 ns. A detailed description of the SNSPDs and associated setup is provided in Section 8.6.

The MZI has a path length difference of 2 ns and is used to perform projection measurements of $|e\rangle_B$, $|l\rangle_B$, and $(|e\rangle_B + e^{i\varphi}|l\rangle_B)/\sqrt{2}$, by detecting photons at three distinct arrival times in one of the outputs, and varying the relative phase φ [28]. Detection at the other output yields the same measurements except with a relative phase of $\varphi + \pi$. Using a custom temperature-feedback system, we slowly vary φ for up to 15 hour time intervals to collect all measurements, which is within the cryostat hold time. Further details of the MZI setup is described in Section 8.6.

Charlie: Bell-state measurement

Charlie consists of a 50/50 polarization-maintaining fiber beam splitter (BS), with relevant photons from the Alice and Bob subsystems directed to each of its inputs via a PBSs and optical fiber. The photons are detected at each output with an SNSPD after HPFs, with their arrival times recorded using the DAQ as was done at Bob. Teleportation is facilitated by measurement of the $|\Psi^-\rangle_{AB} = (|el\rangle_{AB} - |le\rangle_{AB})/\sqrt{2}$ Bell state, which corresponds to the detection of a photon in $|e\rangle$ at one detector followed by the detection of a photon in $|l\rangle$ at the other detector after Alice and Bob's (indistinguishable) qubits arrive at the BS [54]. Projection on the $|\Psi^-\rangle_{AB}$ state corresponds to teleportation of $|A\rangle$ up to a known local unitary transformation, i.e., our system produces $-i\sigma_y |A\rangle$, with σ_y being the Pauli y-matrix.

8.3 Experimental results

Prior to performing quantum teleportation, we measure some key parameters of our system that underpin the teleportation fidelity. Specifically, we determine the fidelity of the entangled state produced by Bob by measuring the entanglement visibility V_{ent} [55], and also determine to what extent Alice and Bob's photons are indistinguishable at Charlie's BS using the HOM effect [47].

Entanglement visibility

The state $|pair\rangle_B$ (and hence the entangled state $|\phi^+\rangle_B$) described in Sec. 8.2 is idealized. In reality, the state produced by Bob is better approximated by a two-mode squeezed vacuum state $|\text{TMSV}\rangle_B = \sqrt{1-p}\sum_{n=0}^{\infty}\sqrt{p}^n\,|nn\rangle_B$ after the FBG filter and neglecting loss [56]. Here, n is the number of photons per temporal mode (or qubit), p is the emission probability of a single pair per mode (or qubit), with state ordering referring to signal and idler modes. However, $|\text{TMSV}\rangle_B$ approximates a photon pair for $p \ll 1$, with $p \approx \mu_B$ mean number of pairs per mode (or qubit), conditioned on measurement of a pair such that the $n = 0$ term is eliminated. As a compromise between the pair-creation rate $\propto p$ and the quality of entanglement, here and henceforth we set the mean photon number of our pair source to be $\mu_B = (8.0 \pm 0.4) \times 10^{-3}$ per time bin, which is feasible because of the exceptionally low dark counts of our SNSPDs. The measurement of μ_B is outlined in Section 8.6.

We generate $|\phi^+\rangle_B$ and measure V_{ent} by directing the idler photon to the second input port of the MZI, slightly modifying the setup of Fig. 8.1. The idler photon is delayed compared to the signal, allowing unambiguous measurement of each qubit. We vary φ and project each qubit of the entangled state onto phase-varied superpositions of $|e\rangle$ and $|l\rangle$ by accumulating coincidence events of photons at both the outputs of the interferometer [55].

The results shown in Fig. 8.2 are fit proportional to $1 + V_{ent}\sin(\omega T + \Phi)$, where $V_{ent} = (R_x - R_n)/(R_x + R_n)$, with $R_{x(n)}$ denoting the maximum (minimum) rate of coincidence events [55], ω and Φ are unconstrained constants, and T is the temperature of the MZI, finding $V_{ent} = 96.4 \pm 0.3\%$.

The deviation from unit visibility is mainly due to non-zero multi photon emissions [57], which is supported by an analytical model that includes experimental imperfections (see Chapter 9). Nonetheless, this visibility is far beyond the $1/3$ required for non-separability of a Werner state [58] and the locality bound of $1/\sqrt{2}$ [59, 55]. Furthermore, it predicts a fidelity $F_{ent} = (3V_{ent} + 1)/4 = 97.3 \pm .2\%$ with respect to $|\phi^+\rangle$ [58], and hence is sufficient for quantum teleportation.

HOM interference visibility

The BSM relies on quantum interference of photons from Alice and Bob. This is ensured by the BS at Charlie, precise control of the arrival time of photons with IMs, identical FBG filters, and POCs (with PBSs) to provide the required indistinguishabiliy. The degree of interference is quantified by way of the HOM interference

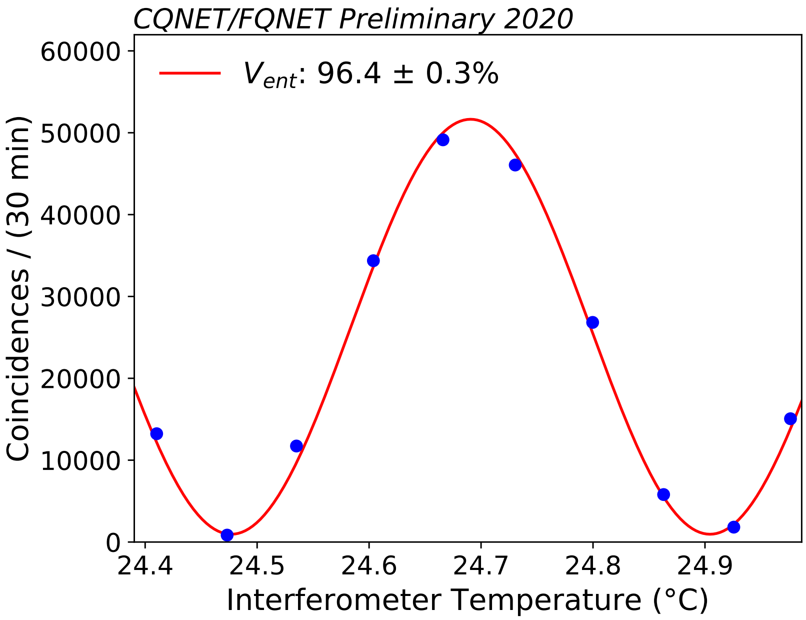

Figure 8.2: Entanglement visibility. The temperature of the interferometer is varied to reveal the expected sinusoidal variations in the rate of coincidence events. A fit reveals the entanglement visibility $V_{ent} = 96.4 \pm 0.3\%$, see main text for details. Uncertainties here and in all measurements are calculated assuming Poisson statistics.

visibility $V_{HOM} = (R_d - R_i)/R_d$, with $R_{d(i)}$ denoting the rate of coincident detections of photons after the BS when the photons are rendered as distinguishable (indistinguishable) as possible [47]. Completely indistinguishable single photons from Alice and Bob may yield $V_{HOM} = 1$. However in our system, Alice's qubit is approximated from a coherent state $|\alpha\rangle_A = \mathrm{e}^{-|\alpha|^2/2} \sum_{n=0}^{\infty} \frac{\alpha^n}{\sqrt{n!}} |n\rangle_A$ with $\alpha \ll 1$, akin to how Bob's pair is approximated from $|\mathrm{TMSV}\rangle_B$ (see Sec. 8.3), with $\mu_A = |\alpha|^2$ being Alice's mean photon number per mode (or qubit) [56]. Therefore, the contribution of undesired photons from Alice and Bob lowers the maximum achievable V_{HOM} below unity, with a further reduction if the interfering photons are not completely indistinguishable. The dependence of V_{HOM} with varied μ_A and μ_B, including effects of losses or distinguishable photons in our system is analytically modeled in Chapter 9, and briefly discussed in Sec. 8.4.

We measure V_{HOM} by slightly modifying the setup of Fig. 8.1: We prepare $|A\rangle = |e\rangle_A$ with $\mu_A = 2.6 \times 10^{-3}$ and Bob as $|pair\rangle_B$ and direct Alice's photon and Bob's idler to Charlie, with Bob's signal bypassing the MZI to be directly measured by an SNSPD. Alice's IM is used to introduce distinguishability by way of a relative difference in arrival time Δt_{AB} of Alice and Bob's photons at Charlie's BS. Using

Charlie's SNSPDs and the third detector at Bob, a three-fold coincidence detection rate is measured for varying Δt_{AB}, with results shown in Fig. 8.3a. Since the temporal profiles of our photons are approximately Gaussian, we fit our results to $A[1 - V_{HOM}\exp\left(-\frac{\Delta t_{AB}^2}{2\sigma^2}\right)]$, where A is the maximum coincidence rate when the photons are completely distinguishable and $\sigma = 300$ ps is the $1/e$ temporal duration of the optical pulses [47, 60], finding $V_{HOM} = 70.9 \pm 1.9\%$. The maximum V_{HOM} for this experiment is 83.5% if the photons were completely indistinguishable (see Chapter 9), with the difference ascribed to slight distinguishability between our photons as supported by the further measurements and analytical modeling in Sec. 8.4. Improvements to our system to remove this distinguishability is discussed in Sec. 8.5.

To test our system for quantum teleportation over long distances, we introduce the aforementioned 22, 11, and 11 km lengths of single-mode fiber between Alice and Charlie, Bob and Charlie, and in the path of Bob's signal photon, respectively, repeat our measurement of V_{HOM} and fit the results as before (see Fig. 8.3b). We find $V_{HOM} = 63.4 \pm 5.9\%$, which is consistent with the maximum V_{HOM} we expect when including the impact of the additional 5.92 (2.56) dB loss between Charlie and Alice (Bob) as well as the effect of photon distinguishability (analyzed in Sec. 8.4). This suggests that the additional fiber importantly does not introduce any further distinguishability (that we cannot account for), thereby supporting our system's use in quantum networking. Overall, the presence of clear HOM interference suggests our system (with or without the additional fiber) introduces relatively little imperfections that can negatively impact the BSM and hence the fidelity of quantum teleportation.

Quantum teleportation

We now perform quantum teleportation of the time-bin qubit basis states $|e\rangle$, $|l\rangle$ and $|+\rangle$, so as to measure the teleportation fidelities, F_e, F_l, an F_+, respectively, of the teleported states with respect to their ideal counterparts, up to the local unitary introduced by the BSM (see Sec. 8.2). Since measurement of $|+\rangle$ in our setup by symmetry is equivalent to any state of the form $(|e\rangle + e^{i\varphi}|l\rangle)/\sqrt{2}$ (and in particular the remaining three basis states $(|e\rangle - |l\rangle)/\sqrt{2}$ and $(|e\rangle \pm i\,|l\rangle)/\sqrt{2}$), we may determine the average teleportation fidelity $F_{avg} = (F_e + F_l + 4F_+)/6$ of any time-bin qubit.

First, we prepare $|e\rangle_A$ and $|l\rangle_A$ with $\mu_A = 3.53\times10^{-2}$, with Bob's idler bypassing the

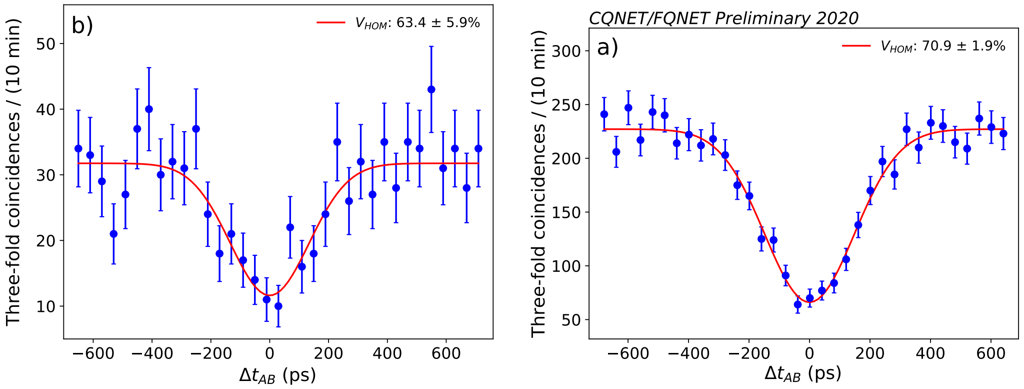

Figure 8.3: Hong-Ou-Mandel (HOM) interference. A relative difference in arrival time is introduced between photons from Alice and Bob at Charlie's BS. HOM interference produces a reduction of the three-fold coincidence detection rate of photons as measured with SNSPDs after Charlie's BS and at Bob. A fit reveals a) $V_{HOM} = 70.9 \pm 1.9\%$ and b) $V_{HOM} = 63.4 \pm 5.9\%$ when lengths of fiber are added, see main text for details.

MZI to be detected by a single SNSPD. We measure $F_e = 95 \pm 1\%$ and $F_l = 96 \pm 1\%$, conditioned on a successful measurement of $|\Psi^-\rangle_{AB}$ at Charlie, with fidelity limited by multiphoton events in Alice and Bob's qubits and dark counts of the SNSPDs (see Chapter 9). We then repeat the measurement with $\mu_A = 9.5 \times 10^{-3}$ after inserting the aforementioned 44 km length of fiber as before to emulate Alice, Charlie and parts of Bob being separated by long distances. This gives $F_e = 98 \pm 1\%$ and $F_l = 98 \pm 2\%$, with no reduction from the additional fiber loss owing to our low noise SNSPDs.

Next, we prepare $|+\rangle_A$ with $\mu_A = 9.38 \times 10^{-3}$, insert the MZI and, conditioned on the BSM, we measure $F_+ = (1 + V_+)/2 = 84.9 \pm 0.5\%$ by varying φ. Here, $V_+ = 69.7 \pm 0.9\%$ is the average visibility obtained by fits to the resultant interference measured at each output of the MZI, as shown in Fig. 8.4a. The reduction in fidelity from unity is due to multiphoton events and distinguishability, consistent with that inferred from HOM interference, as supported by further measurements and analytical modeling in Sec. 8.4.

The measurement is repeated with the additional long fiber, giving $V_+ = 58.6 \pm 5.7\%$ and $F_+ = 79.3 \pm 2.9\%$ with results and corresponding fit shown in Fig. 8.4b. The reduced fidelity is likely due to aforementioned polarization variations over the long fibers, consistent with the reduction in HOM interference visibility, and exacerbated here owing to the less than ideal visibility of the MZI over long measurement times (see Sec. 8.6).

The results yield $F_{avg} = 89 \pm 1\%$ ($86 \pm 3\%$) without (with) the additional fiber, which is significantly above the classical bound of $2/3$, implying strong evidence of quantum teleportation [61], and limited from unity by multiphotons events, distinguishability, and polarization variations, as mentioned in Chapter 9.

To glean more information about our teleportation system beyond the fidelity, we reconstruct the density matrices of the teleported states using a maximum-likelihood QST [48] described in Section 8.6. The results of the QST with and without the additional fiber lengths are summarized in Figs. 8.8a and b, respectively. As can be seen, the diagonal elements for $|+\rangle$ are very close to the expected value indicating the preservation of probabilities for the basis states of $|e\rangle$ and $|l\rangle$ after teleportation, while the deviation of the off-diagonal elements indicate the deterioration of coherence between the basis states. The decoherence is attributed to multiphoton emissions from our entangled pair source and distinguishability, consistent with the aforementioned teleportation fidelities of $|+\rangle_A$, and further discussed in Sec. 8.4. Finally, we do also extract the teleportation fidelity from these density matrices, finding the results shown in Fig. 8.5, and $F_{avg} = 89 \pm 1\%$ ($88 \pm 3\%$) without (with) the fiber spools, which are consistent with previous measurements given the similar μ_A used for QST.

We point out that the $2/3$ classical bound may only be applied if Alice prepares her qubits using genuine single photons, i.e., $|n = 1\rangle$, rather than using $|\alpha \ll 1\rangle$ as we do in this work [62]. As a way to account for the photon statistics of Alice's qubits we turn to an analysis using decoy states.

Teleportation fidelity using decoy states

To determine the minimum teleportation fidelity of qubits prepared using single photons, we use a decoy state method [49] and follow the approach of Refs. [63, 29]. Decoy states, which are traditionally used in quantum key distribution to defend against photon-number splitting attacks, are qubits encoded into coherent states $|\alpha\rangle$ with varying mean photon number $\mu_A = |\alpha|^2$. Measuring fidelities of the teleported qubits for different μ_A, the decoy-state method allows us to calculate a lower bound F_A^d on the teleportation fidelity if Alice had encoded her qubits using $|n = 1\rangle$.

We prepare decoy states $|e\rangle_A$, $|l\rangle_A$, and $|+\rangle_A$ with varying μ_A, as listed in Table 8.1, and perform quantum teleportation both with and without the added fiber, with

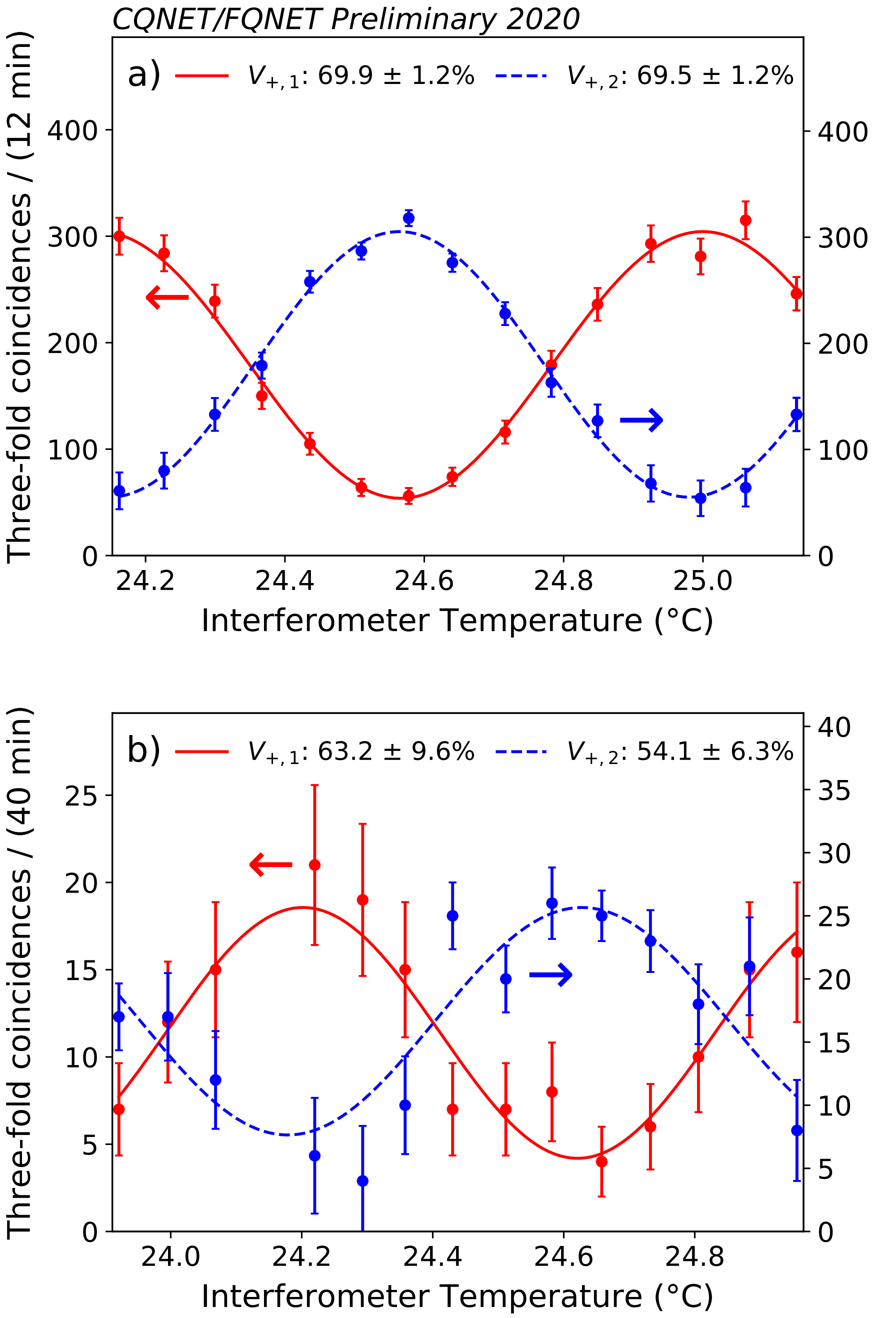

Figure 8.4: Quantum teleportation of $|+\rangle$. Teleportation is performed b) with and a) without an additional 44 km of single-mode fiber inserted into the system. The temperature of the inteferometer is varied to yield a sinusoidal variation of the three-fold coincidence rate at each output of the MZI (blue and red points). A fit of the visibilities (see Sec. 8.3) measured at each output ($V_{+,1}$, $V_{+,2}$) of the MZI gives an average visibility $V_{+} = (V_{+,1} + V_{+,2})/2$ of a) 69.7 ± 0.91% without the additional fiber and b) 58.6 ± 5.7% with the additional fiber.

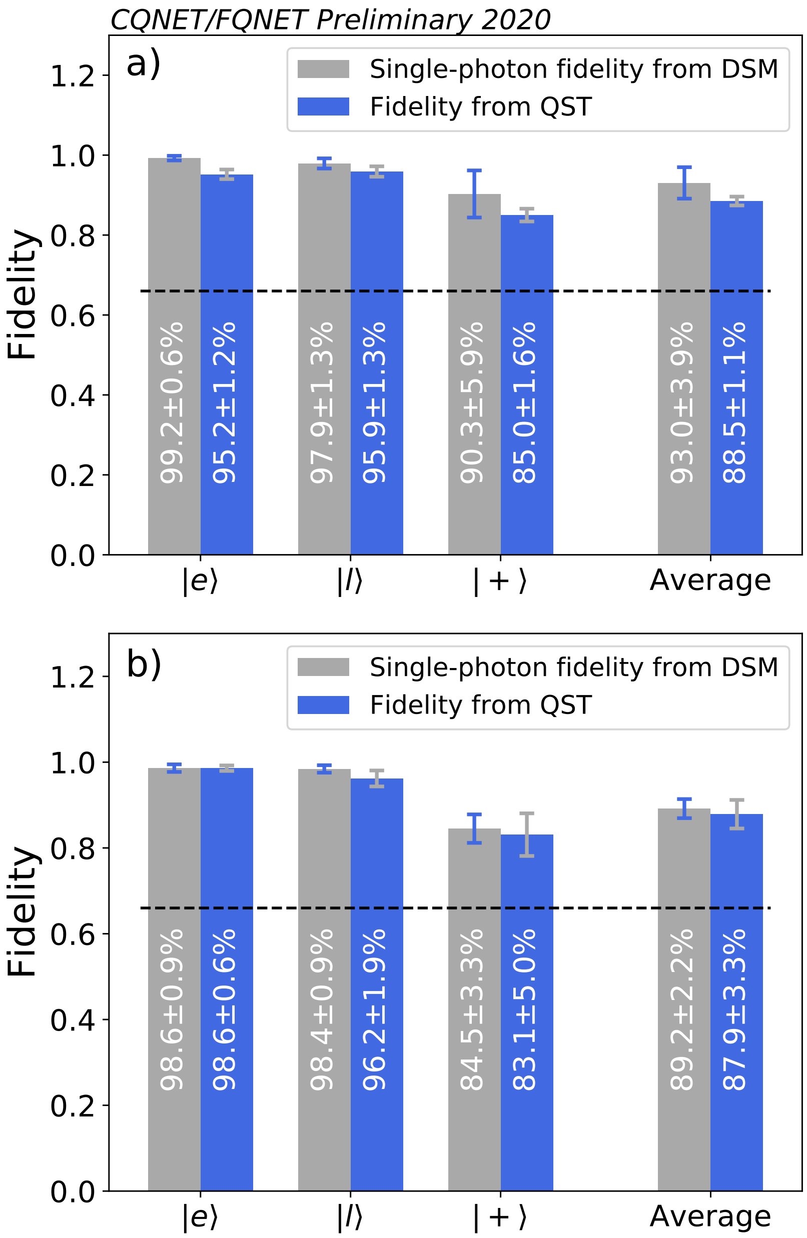

Figure 8.5: Quantum teleportation fidelities for $|e\rangle_A$, $|l\rangle_A$, and $|+\rangle_A$, including the average fidelity. The dashed line represents the classical bound. Fidelities using quantum state tomography (QST) are shown using blue bars while the minimum fidelities for qubits prepared using $|n=1\rangle$, F_e^d, F_l^d, and F_+^d, including the associated average fidelity F_{avg}^d, respectively, using a decoy state method (DSM) is shown in grey. Panels a) and b) depicts the results without and with additional fiber, respectively. Uncertainties are calculated using Monte-Carlo simulations with Poissonian statistics.

teleportation fidelities shown in Table 8.1. From these results we calculate F_A^d as shown in Fig. 8.5, with $F_{avg}^d \geq 93 \pm 4\%$ ($F_{avg}^d \geq 89 \pm 2\%$) without (with) the added fiber, which significantly violate the classical bound and the bound of $5/6$ given by an optimal symmetric universal cloner [64, 65], clearly demonstrating the capability of our system for high-fidelity teleportation. As depicted in Fig. 8.5 these fidelities nearly match the results we obtained without decoy states within statistical uncertainty. This is due to the suitable μ_A, as well as low μ_B and SNSPD dark counts in our previous measurements (see Chapter 9).

qubit	without long fiber		with long fiber	
	μ_A ($\times 10^{-3}$)	F_A^d (%)	μ_A ($\times 10^{-3}$)	F_A^d (%)
$\vert e\rangle_A$	3.53	95.2 ± 1	26.6	95.7 ± 1.5
	1.24	86.7 ± 2	9.01	98.4 ± 1.1
	0	52.8 ± 3.4	-	-
$\vert l\rangle_A$	3.53	95.9 ± 1	32.9	98.6 ± 0.7
	1.24	90.5 ± 2	9.49	98.4 ± 1.6
	0	52.8 ± 3.4	-	-
$\vert +\rangle_A$	9.38	84.7 ± 1.1	29.7	73.6 ± 3.0
	2.01	83.2 ± 3.6	10.6	82.21 ± 3.9
	0	52.8 ± 3.4	-	-

Table 8.1: Teleportation fidelities with (right column) and without (center column) the 44 km-length of fiber for Alice's qubit states prepared with varying μ_A. Mean photon numbers and fidelities for vacuum states with fiber are assumed to be zero and 50%, respectively.

8.4 Analytical model and simulation

As our measurements have suggested, multi-photon components in, and distinguishability between, Alice and Bob's qubits reduce the values of key metrics including HOM interference visibility and, consequently, quantum teleportation fidelity. To capture these effects in our model, we employ a Gaussian-state characteristic-function method developed in Chapter 9, which was enabled by work in Ref. [66]. This approach is well-suited to analyze our system because the quantum states, operations, and imperfections (including losses, dark counts, etc.) of the experiment can be fully described using Gaussian operators, see e.g., Ref. [67]. We now briefly outline the model of Chapter 9, and employ it to estimate the amount of indistinguishability ζ between Alice and Bob's qubits in our measurements of HOM interference and quantum teleportation.

The distinguishability in any degree-of-freedom may be modeled by introducing a virtual beam splitter of transmittance ζ into the paths of Alice and Bob's relevant photons. As shown in Fig. 8.6, indistinguishable components of incoming photon modes are directed towards Charlie's BS where they interfere, whereas distinguishable components are mixed with vacuum at the BS and do not contribute to interference. Here $\zeta = 1$ ($\zeta = 0$) corresponds to the case when both incoming photons are perfectly indistinguishable (distinguishable). Now we may calculate the probability of a three-fold coincidence detection event P_{3f} between D_1, D_2 (Charlies' detectors), and D_3 (detects Bob's signal photon) for a given qubit state ρ_{AB} from Alice and Bob:

$$\begin{aligned} P_{3f} = \mathrm{Tr}\{\rho_{AB}(\mathbb{I} - (|0\rangle\langle 0|)^{\otimes 3}_{\hat{a}_1,\hat{a}_2,\hat{a}_3}) \\ \otimes (\mathbb{I} - (|0\rangle\langle 0|)^{\otimes 3}_{\hat{b}_1,\hat{b}_2,\hat{b}_3}) \otimes (\mathbb{I} - (|0\rangle\langle 0|)_{\hat{c}})\}, \end{aligned} \tag{8.1}$$

where the $\hat{a}$ and $\hat{b}$ operators refer to modes, which originate from Alice and Bob's virtual beam splitters and are directed to D_1 and D_2, respectively, and $\hat{c}$ corresponds to Bob's idler mode, which is directed to D_3, see Fig. 8.6. This allows the derivation

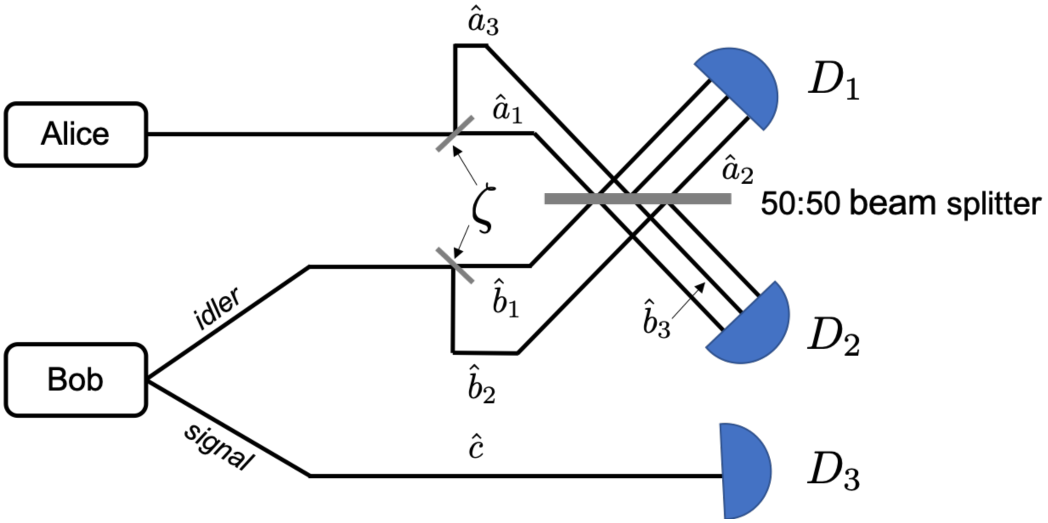

Figure 8.6: Schematic depiction of distingushability between Alice and Bob's photons at Charlie's BS. Distinguishability is modeled by means of a virtual beam splitter with a transmittance ζ. Indistinguishable photons contribute to interference at the Charlie's BS while distinguishable photons are mixed with vacuum, leading to a reduction of HOM visibility and teleportation fidelity. See main text for further details.

of an expression for the HOM interference visibility

$$V_{HOM}(\zeta) = [P_{3f}(0) - P_{3f}(\zeta)]/P_{3f}(0), \tag{8.2}$$

consistent with that introduced in Sec. 8.3. Since Alice and Bob ideally produce $\rho_{AB} = (|\alpha\rangle\langle\alpha|) \otimes (|\text{TMSV}\rangle\langle\text{TMSV}|)$, and recognizing that all operators in P_{3f} are Gaussian, we analytically derive

$$\begin{aligned} P_{3f}(\zeta) = 1 - 2&\frac{\exp\left(-\frac{\mu_A/2[1+(1-\zeta^2)\eta_i\mu_B/2]}{1+\eta_i\mu_B/2}\right)}{1+\eta_i\mu_B/2} \\ &- \frac{1}{1+\eta_s\mu_B} + \frac{\exp(-\mu_A)}{1+\eta_i\mu_B} \\ &- \frac{\exp(-\mu_A)}{1+(1-\eta_s)\eta_i\mu_B+\eta_s\mu_B} \\ &+ 2\frac{\exp\left(-\frac{\mu_A/2[1+(1-\zeta^2)(1-\eta_s)\eta_i\mu_B/2+\eta_s\mu_B]}{1+(1-\eta_s)\eta_i\mu_B/2+\eta_s\mu_B}\right)}{1+(1-\eta_s)\eta_i\mu_B/2+\eta_s\mu_B}, \end{aligned} \tag{8.3}$$

for varied ζ, where η_i and η_s are the transmission efficiencies of the signal and idler photons, including detector efficiencies. We similarly calculate the impact of distinguishability on the teleportation fidelity of $|+\rangle$:

$$F(\zeta) = P_{3f}(\zeta, \varphi_{max})/[P_{3f}(\zeta, \varphi_{max}) + P_{3f}(\zeta, \varphi_{min})], \tag{8.4}$$

where φ_{max} (φ_{min}) is the phase of the MZI added into the path of the signal photon, corresponding to maximum (minimum) three-fold detection rates.

To compare the model to our measurements, we use the experimental mean photon numbers for the photon-pair source $\eta_i = 1.2 \times 10^{-2}$ and $\eta_s = 4.5 \times 10^{-3}$ as determined by the method described in Section 8.6. We then measure the teleportation fidelity of $|+\rangle$ and HOM interference visibility (keeping the MZI in the system to ensure η_s remains unchanged) for different values μ_A. The results are plotted in Fig. 8.7. The data is then fitted to the expressions $V_{HOM}(\zeta)$ and $F(\zeta)$ derived in our model and graphed in Fig. 8.7. The fitted curves are in very good agreement with our experimental values and consistently yield a value of $\zeta = 90\%$ for both measurements types. This implies that we have only a small amount of residual distinguishability between Alice and Bob's photons. Potential effects leading to this distinguishability are discussed in Sec. 8.5.

Overall, our analytic model is consistent with our experimental data (see Chapter 9) in the regime of $\mu_A \ll 1$, which is the parameter space most often used in quantum

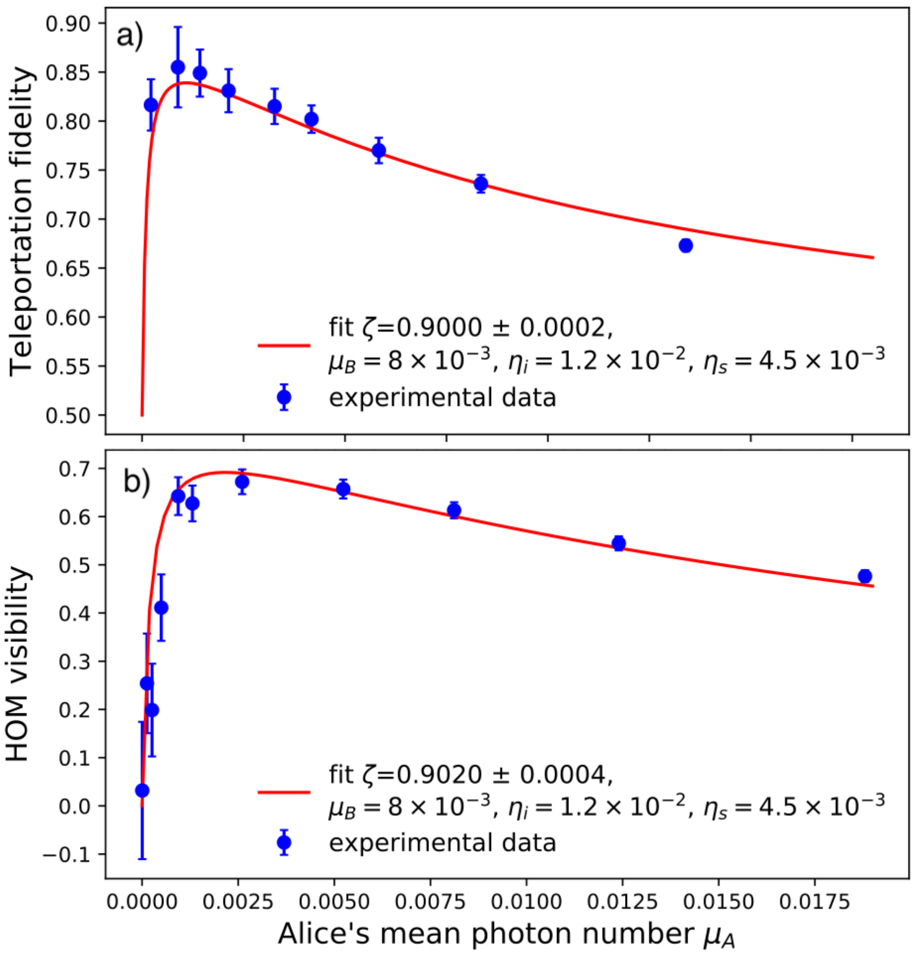

Figure 8.7: Evaluation of photon indistinguishability using an analytical model. Panel a) depicts the quantum teleportation fidelity of $|+\rangle$ while panel b) shows the HOM interference visibility, each with varied mean photon number μ_A of Alice's qubits. Fits of analytical models the data reveal $\zeta = 90\%$ indistinguishability between Alice and Bob's photons at Charlie's BS. Bob produces μ_B photon pairs on average, η_i and η_s are the probabilities for an individual idler (signal) photon to arrive at Charlie's BS and be detected at Bob's detector, respectively.

networking protocols (e.g., key distribution). Our model, thus, offers a practical way to determine any underlying distinguishability in a deployed network where a full characterization of the properties of Alice and Bob's photons may not be possible.

8.5 Discussion

We have demonstrated quantum teleportation systems for photonic time-bin qubits at a quantum channel- and device-compatible wavelength of 1536.5 nm using a fiber-based setup comprising off-the-shelf components and state-of-the-art SNSPDs. We measure an average fidelity above 90% using QST and a decoy state analysis with up to 44 km of single mode fiber in our setup. Our results are further supported by an analytical model in conjunction with measurements of the entanglement and HOM interference visibilities.

The decoy state analysis indicates that the maximum teleportation fidelity is currently restricted by that of the teleported qubits prepared in superposition states, for which a 10% distinguishability between the qubits undergoing BSM and the contribution of multiple photon pairs play the largest role. Our model predicts that the average fidelity will increase to 95% with completely indistinguishable photons, while fidelities close to unity can be achieved with lowered mean number of photon pairs. Alternatively, we may replace our SNSPDs with efficient photon-number resolving (PNR) SNSPDs [68] to allow postselection of multiphoton events at the MZI or BSM [69]. Nonetheless, both approaches must be accompanied by increased coupling efficiencies of the pair source beyond the current $\sim 1\%$ either to maintain realistic teleportation rates (above the system noise and current rate of phase drift of the MZI), or to derive any advantage from PNR capability.

As suggested by the width of our HOM interference fringe – which predicts an average photon bandwidth of $0.44/\sigma$ ~1.5 GHz (see Sec. 8.3), i.e., less than the 2 GHz bandwidth of our FBGs – the indistinguishability in our system could be limited by the large difference in the bandwidth between the photons originating from the SPDC (>100 GHz) and those generated at Alice by the IM (15 GHz), leading to nonidentical filtering by the FBG. This can be improved by narrower FBGs or by using a more broadband pump at Alice (e.g., using a mode locked laser or a higher bandwidth IM, e.g., > 50 GHz, which is commercially available). Alternatively, pure photon pairs may be generated by engineered phase matching, see, e.g., Ref. [70]. Distinguishability owing to nonlinear modulation during the SHG process could also play a role [71]. The origin of distinguishability in our system, whether due to imperfect filtering or other device imperfections (e.g., PBS or BS) will be studied in future work. Coupling loss can be minimized to less than a few dB overall by improved fiber-to-chip coupling, lower-loss components of the FBGs (e.g., the required isolator), spliced fiber connections, and reduced losses within our MZI. Note that our current coupling efficiency is equivalent to ~50 km of single mode fiber, suggesting that our system is well-suited for quantum networks provided loss is reduced.

While the fidelities we demonstrate are sufficient for several applications, the current ~Hz teleportation rates with the 44 km length of fiber are still low. Higher repetition rates (e.g., using high-bandwidth modulators with wide-band wavelength division multiplexed filters and low-jitter SNSPDs [72]), improvements to coupling and detector efficiencies, enhanced BSM efficiency with fast-recovery SNSPDs [73], or multiplexing in frequency [63] will all yield substantial increases in teleportation rate. Note that increased repetition rates permits a reduction in time bin separation which will allow constructing the MZI on chip, providing exceptional phase stability and hence, achievable fidelity. Importantly, the aforementioned increases in repetition rate and efficiency are afforded by improvements in SNSPD technology that are currently being pursued with our JPL, NIST and other academic partners.

Upcoming system-level improvements we plan to investigate and implement include further automation by the implementation of free-running temporal and polarization feedback schemes to render the photons indistinguishable at the BSM [29, 30]. Furthermore, several electrical components can be miniaturized, scaled, and made more cost effective (e.g., field-programmable gate arrays can replace the AWG).We note that our setup prototype will be easily extended to independent lasers at different locations, also with appropriate feedback mechanisms for spectral overlap [74, 75]. These planned improvements are compatible with the data acquisition and control systems that were built for the systems and experiments at FQNET and CQNET presented in this work.

Overall, our systems for achieving high-fidelity teleportation will serve as a blueprint for the construction of quantum network test-beds and eventually wide-spread quantum networks towards the quantum internet. In this vein, our Fermilab and Caltech Quantum Networks serve as R& D laboratories and prototypes towards real-world quantum networks. The high fidelities achieved in our experiments using practical and replicable devices are essential when expanding a quantum network to many nodes, and enable the realization of more advanced protocols, e.g., Refs. [18, 76, 77].

8.6 Methods

Detailed description of experimental components

Control systems and data acquisition Our system is built with a vision towards future replicability, with particular emphasis on systems integration. Each of the Alice, Bob and Charlie subsystems is equipped with monitoring and active feedback stabilization systems (e.g., for IM extinction ratio), or has capability for remote control of critical network parameters (e.g., varying the qubit generation time). Each subsystem has a central classical processing unit with the following functions: oversight of automated functions and workflows within the subsystem, data acquisition and management, and handling of input and output synchronization streams. As the quantum information is encoded in the time domain the correct operation of the classical processing unit depends critically on the recorded time-of-arrival of the photons at the SNSPDs. Thus significant effort was dedicated to build a robust DAQ subsystem capable of recording and processing large volumes of time-tagged signals from the SNSPDs and recorded by our TDCs at a high rate. The DAQ is designed to enable both real-time data analysis for prompt data quality monitoring as well as post-processing data analysis that allows to achieve the best understanding of the data.

The DAQ system is built on top of the standalone Linux library of our commercial TDC. It records time tags whenever a signal is detected in any channel in coincidence with the reference 90 MHz clock. Time tags are streamed to a PC where they are processed in real-time and stored to disk for future analysis. A graphical user interface has been developed, capable of real-time visualization and monitoring of photons detected while executing teleportation. It also allows for easy control of the time-intervals used for each channel and to configure relevant coincidences between different photon detection events across all TDC channels. We expect our DAQ subsystem to serve as the foundation for future real-world time-bin quantum networking experiments (see Sec. 8.5).

Superconducting nanowire single photon detectors We employ amorphous tungsten silicide SNSPDs manufactured in the JPL Microdevices Laboratory for all measurements at the single photon level (see Sec. 8.2) [52]. The entire detection system is customized for optimum autonomous operation in a quantum network. The SNSPDs are operated at 0.8 K in a closed-cycle sorption fridge [53]. The detectors have nanowire widths between 140 to 160 nm and are biased at a current current of 8 to 9 μA. The full-width at half maximum (FWHM) timing jitter (i.e., temporal resolution) for all detectors is between 60 and 90 ps (measured using a Becker & Hickl SPC-150NXX time-tagging module). The system detection efficiencies (as measured from the fiber bulkhead of the cryostat) are between 76 and 85 %. The SNSPDs feature low dark count rates between 2 and 3 Hz, achieved by short-pass filtering of background black-body radiation through coiling of optical fiber to a 3 cm diameter within the 40 K cryogenic environment, and an additional band-pass filter coating deposited on the detector fiber pigtails (by Andover Corporation). Biasing of the SNSPDs is facilitated by cryogenic bias-Ts with inductive shunts to prevent latching, thus enabling uninterrupted operation. The detection signals are amplified using Mini-Circuits ZX60-P103LN+ and ZFL-1000LN+ amplifiers at room temperature, achieving a total noise figure of 0.61 dB and gain of 39 dB at 1 GHz, which enables the low system jitter. Note that FWHM jitter as low as 45 ps is achievable with the system, by biasing the detectors at approximately 10 μA, at the cost of an elevated DCR on the order of 30 cps. Using commercially available components, the system is readily scalable to as many as 64 channels per cryostat, ideal for star-type quantum networks, with uninterrupted 24/7 operation. The bulkiest component of the current system is an external helium compressor, however, compact rack-mountable versions are readily available [53].

Interferometer and phase stabilization We use a commercial Kylia 04906-MINT MZI, which is constructed of free-space devices (e.g., mirrors, beam splitters) with small form-factor that fits into a hand-held box. Light is coupled into and out of the MZI using polarization maintaining fiber with loss of ~2.5 dB. The interferometer features an average visibility of 98.5% that was determined by directing $|+\rangle$ with $\mu_A = 0.07$ into one of the input ports, measuring the fringe visibility on each of the outputs using an SNSPD. The relative phase φ is controlled by a voltage-driven heater that introduces a small change in refractive index in one arm of the MZI. However, this built-in heater did not permit phase stability sufficient to measure high-fidelity teleportation, with the relative phase following the slowly-varying ambient temperature of the room. To mitigate this instability, we built another casing, thermally isolating the MZI enclosure from the laboratory environment and controlled the temperature via a closed-loop feedback control system based on a commercial thermoelectric cooler and a LTC1923 PID-controller. The temperature feedback is provided by a 10 kΩ NTC thermistor while the set-point is applied with a programmable power supply. This control system permits us to measure visbilities by slowly varying φ over up to 15 hour timescales. We remark that no additional methods of phase control were used beyond that of temperature.

Estimation of mean number of photon pairs and transmission efficiencies of signal and idler photons

Using a method described in Ref. [55], we measure the mean number of photon pairs produced by Bob μ_B as a function of laser excitation power before the PPLN waveguide used for SHG. To this end, we modify the setup of Fig. 8.1 and direct each of Bob's signal and idler photons to a SNSPD. We then measure detection events while varying the amplification of our EDFA by way of an applied current. We extract events when photon pairs which originated from the same clock cycle are measured in coincidence, and when one photon originating from a cycle is measured in coincidence with a photons originated from a preceding or following clock cycle, in other words we measure the so-called coincidence and accidental rates. The ratio of accidentals to coincidences approximates $\mu_B \ll 1$, with all results shown in Table 8.2. For all measurements we use $\mu_B = (8.0 \pm 0.4) \times 10^{-3}$ per time bin, which corresponds to an EDFA current of 600 mA.

The transmission efficiencies of the signal and idler photons, η_s and η_i, respectively, mentioned in Sec. 8.4 are determined by calculating the ratio of the independent rates of detection of the idler and signal photons, respectively, with the coincidence rate of the photons pairs (in the same clock cycle) [55]. We repeat the measurements using the setup shown in Fig. 8.1, which is that used to generate the results of Fig. 8.7 (i.e., we direct the signal and idler photons through the setup as if we are to perform teleportation). We find $\eta_s = 4.5 \times 10^{-3}$ and $\eta_i = 1.2 \times 10^{-2}$, which take into account losses between when the photons are produced to when they are detected by their respective SNSPDs.

EDFA current (mA)	Coincidences (per 10 s)	Accidentals (per 10 s)	μ_B ($\times 10^{-3}$)
400	469.2 ± 3.6	1.8 ± 0.3	3.9 ± 0.7
450	1156.3 ± 4.9	6.1 ± 0.5	5.3 ± 0.4
500	1653.9 ± 5.9	9.5 ± 0.6	5.8 ± 0.4
550	2095.8 ± 6.6	13.7 ± 0.8	6.5 ± 0.4
575	2343.2 ± 7.0	17.7 ± 0.9	7.5 ± 0.4
600	2548.7 ± 7.3	18.5 ± 0.9	8.0 ± 0.4

Table 8.2: Bob's photon pair source is characterized by the measured mean photon number per time bin μ_B, and the rate of accidental and true coincidence detections with varied EDFA current.

Quantum state tomography

We perform projection measurements on the teleported states $|e\rangle_A$, $|l\rangle_B$, and $|+\rangle_A$, in all three of the qubit bases formed by the Pauli matrices $\sigma_x, \sigma_y,$ and σ_z, i.e., measuring photons at each of the arrival times after the MZI and varying φ. These results allow reconstructing the density matrix of each teleported state, both with and without the additional 44 km fiber, using maximum likelihood estimation [48]. Our resultant matrices clearly match the expected teleported state, with the calculated high teleportation fidelities in Sec. 8.3, up to the aforementioned effects due to multiple photons and distinguishability.

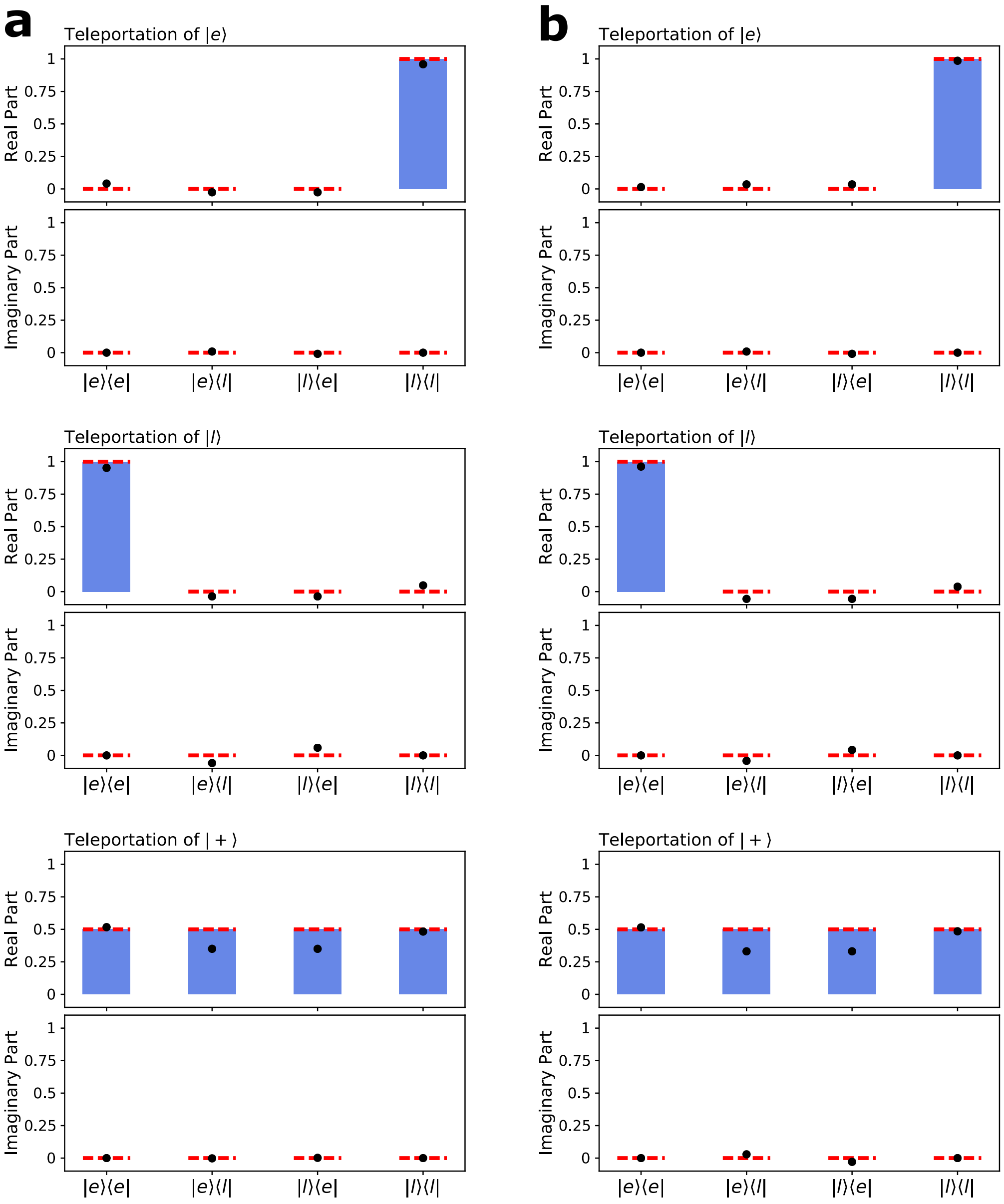

Figure 8.8: Elements of the density matrices of teleported $|e\rangle$, $|l\rangle$, and $|+\rangle$ states a) with and b) without the additional 44 km of fiber in the system. The black points are generated by our teleportation system and the blue bars with red dashed lines are the values assuming ideal teleportation.

References

[1] Charles H. Bennett, Gilles Brassard, Claude Crépeau, Richard Jozsa, Asher Peres, and William K. Wootters. "Teleporting an unknown quantum state via dual classical and Einstein-Podolsky-Rosen channels." In: Physical Review Letters 70.13 (1993), p. 1895.

[2] Dirk Bouwmeester, Jian-Wei Pan, Klaus Mattle, Manfred Eibl, Harald Weinfurter, and Anton Zeilinger. "Experimental quantum teleportation." In: Nature 390.6660 (1997), pp. 575–579.

[3] Danilo Boschi, Salvatore Branca, Francesco De Martini, Lucien Hardy, and Sandu Popescu. "Experimental realization of teleporting an unknown pure quantum state via dual classical and Einstein-Podolsky-Rosen channels." In: Physical Review Letters 80.6 (1998), p. 1121.

[4] Akira Furusawa, Jens Lykke Sørensen, Samuel L Braunstein, Christopher A Fuchs, H Jeff Kimble, and Eugene S Polzik. "Unconditional quantum teleportation." In: Science 282.5389 (1998), pp. 706–709.

[5] B. Hensen, H. Bernien, A. E. Dréau, et al. "Loophole-free Bell inequality violation using electron spins separated by 1.3 kilometres." In: Nature 526.7575 (Oct. 2015), pp. 682–686. ISSN: 1476-4687. DOI: `10.1038/nature15759`. URL: `https://doi.org/10.1038/nature15759`.

[6] Lynden K. Shalm, Evan Meyer-Scott, Bradley G. Christensen, et al. "Strong Loophole-Free Test of Local Realism." In: Physical Review Letters 115 (25 Dec. 2015), p. 250402. DOI: `10.1103/PhysRevLett.115.250402`. URL: `https://link.aps.org/doi/10.1103/PhysRevLett.115.250402`.

[7] Marissa Giustina, Marijn A. M. Versteegh, Sören Wengerowsky, et al. "Significant-Loophole-Free Test of Bell's Theorem with Entangled Photons." In: Physical Review Letters 115 (25 Dec. 2015), p. 250401. DOI: `10.1103/PhysRevLett.115.250401`. URL: `https://link.aps.org/doi/10.1103/PhysRevLett.115.250401`.

[8] Wenjamin Rosenfeld, Daniel Burchardt, Robert Garthoff, Kai Redeker, Norbert Ortegel, Markus Rau, and Harald Weinfurter. "Event-Ready Bell Test Using Entangled Atoms Simultaneously Closing Detection and Locality Loopholes." In: Physical Review Letters 119 (1 July 2017), p. 010402. DOI: `10.1103/PhysRevLett.119.010402`. URL: `https://link.aps.org/doi/10.1103/PhysRevLett.119.010402`.

[9] Ping Gao, Daniel Louis Jafferis, and Aron C Wall. "Traversable wormholes via a double trace deformation." In: Journal of High Energy Physics 2017.12 (2017), p. 151.

[10] Beni Yoshida and Norman Y Yao. "Disentangling scrambling and decoherence via quantum teleportation." In: Physical Review X 9.1 (2019), p. 011006.

[11] Kevin A. Landsman, Caroline Figgatt, Thomas Schuster, Norbert M. Linke, Beni Yoshida, Norm Y. Yao, and Christopher Monroe. "Verified quantum information scrambling." In: Nature 567.7746 (2019), pp. 61–65.

[12] Seth Lloyd, Lorenzo Maccone, Raul Garcia-Patron, et al. “Closed Timelike Curves via Postselection: Theory and Experimental Test of Consistency.” In: Physical Review Letters 106 (4 Jan. 2011), p. 040403. DOI: `10.1103/PhysRevLett.106.040403`. URL: `https://link.aps.org/doi/10.1103/PhysRevLett.106.040403`.

[13] Markus Aspelmeyer, Tobias J Kippenberg, and Florian Marquardt. “Cavity optomechanics.” In: Reviews of Modern Physics 86.4 (2014), p. 1391.

[14] P-Y Hou, Y-Y Huang, X-X Yuan, X-Y Chang, Chong Zu, Li He, and L-M Duan. “Quantum teleportation from light beams to vibrational states of a macroscopic diamond.” In: Nature communications 7 (2016), p. 11736.

[15] Michael A. Nielsen and Isaac L. Chuang. Quantum Computation and Quantum Information. 10th ed. USA: Cambridge University Press, 2011. ISBN: 1107002176.

[16] Thaddeus D Ladd, Fedor Jelezko, Raymond Laflamme, Yasunobu Nakamura, Christopher Monroe, and Jeremy Lloyd O’Brien. “Quantum computers.” In: Nature 464.7285 (2010), pp. 45–53.

[17] Nicolas Gisin and Rob Thew. “Quantum communication.” In: Nature Photonics 1.3 (2007), p. 165.

[18] Stefano Pirandola, Jens Eisert, Christian Weedbrook, Akira Furusawa, and Samuel L. Braunstein. “Advances in quantum teleportation.” In: Nature Photonics 9.10 (2015), p. 641.

[19] H-J Briegel, Wolfgang Dür, Juan I. Cirac, and Peter Zoller. “Quantum repeaters: the role of imperfect local operations in quantum communication.” In: Physical Review Letters 81.26 (1998), p. 5932.

[20] H Jeff Kimble. “The quantum internet.” In: Nature 453.7198 (2008), pp. 1023–1030.

[21] Christoph Simon. “Towards a global quantum network.” In: Nature Photonics 11.11 (2017), pp. 678–680.

[22] Stephanie Wehner, David Elkouss, and Ronald Hanson. “Quantum internet: A vision for the road ahead.” In: Science 362.6412 (2018), eaam9288.

[23] Nicolas Sangouard, Christoph Simon, Hugues De Riedmatten, and Nicolas Gisin. “Quantum repeaters based on atomic ensembles and linear optics.” In: Reviews of Modern Physics 83.1 (2011), pp. 33–80.

[24] Josephine Dias and Timothy C. Ralph. “Quantum repeaters using continuous-variable teleportation.” In: Physical Review A 95.2 (2017), p. 022312.

[25] Marco Lucamarini, Zhiliang L. Yuan, James F. Dynes, and Andrew J. Shields. “Overcoming the rate–distance limit of quantum key distribution without quantum repeaters.” In: Nature 557.7705 (2018), pp. 400–403.

[26] M. K. Bhaskar, R. Riedinger, B. Machielse, et al. "Experimental demonstration of memory-enhanced quantum communication." In: Nature 580.7801 (Apr. 2020), pp. 60–64. ISSN: 1476-4687. DOI: `10.1038/s41586-020-2103-5`. URL: `https://doi.org/10.1038/s41586-020-2103-5`.

[27] Xiu-Xiu Xia, Qi-Chao Sun, Qiang Zhang, and Jian-Wei Pan. "Long distance quantum teleportation." In: Quantum Science and Technology 3.1 (2017), p. 014012.

[28] Jürgen Brendel, Nicolas Gisin, Wolfgang Tittel, and Hugo Zbinden. "Pulsed energy-time entangled twin-photon source for quantum communication." In: Physical Review Letters 82.12 (1999), p. 2594.

[29] Raju Valivarthi, Marcelli Grimau Puigibert, Qiang Zhou, Gabriel H. Aguilar, Varun B. Verma, Francesco Marsili, Matthew D. Shaw, Sae Woo Nam, Daniel Oblak, and Wolfgang Tittel. "Quantum teleportation across a metropolitan fibre network." In: Nature Photonics 10.10 (Oct. 2016), pp. 676–680. ISSN: 1749-4893. DOI: `10.1038/nphoton.2016.180`. URL: `https://doi.org/10.1038/nphoton.2016.180`.

[30] Qi-Chao Sun, Ya-Li Mao, Si-Jing Chen, et al. "Quantum teleportation with independent sources and prior entanglement distribution over a network." In: Nature Photonics 10.10 (Oct. 2016), pp. 671–675. ISSN: 1749-4893. DOI: `10.1038/nphoton.2016.179`. URL: `https://doi.org/10.1038/nphoton.2016.179`.

[31] Hiroki Takesue and Benjamin Miquel. "Entanglement swapping using telecom-band photons generated in fibers." In: Opt. Express 17.13 (June 2009), pp. 10748–10756.

[32] Sheng-Kai Liao, Hai-Lin Yong, Chang Liu, et al. "Long-distance free-space quantum key distribution in daylight towards inter-satellite communication." In: Nature Photonics 11.8 (Aug. 2017), pp. 509–513. ISSN: 1749-4893. DOI: `10.1038/nphoton.2017.116`. URL: `https://doi.org/10.1038/nphoton.2017.116`.

[33] Alexander I. Lvovsky, Barry C. Sanders, and Wolfgang Tittel. "Optical quantum memory." In: Nature Photonics 3.12 (2009), p. 706.

[34] Nikolai Lauk, Neil Sinclair, Shabir Barzanjeh, Jacob P Covey, Mark Saffman, Maria Spiropulu, and Christoph Simon. "Perspectives on quantum transduction." In: Quantum Science and Technology 5.2 (2020), p. 020501.

[35] Nicholas J. Lambert, Alfredo Rueda, Florian Sedlmeir, and Harald G. L. Schwefel. "Coherent conversion between microwave and optical photons—an overview of physical implementations." In: Advanced Quantum Technologies 3.1 (2020), p. 1900077.

[36] Vladimir B. Braginsky and F. Ya Khalili. "Quantum nondemolition measurements: the route from toys to tools." In: Reviews of Modern Physics 68.1 (1996), p. 1.

[37] Ivan Marcikic, Hugues De Riedmatten, Wolfgang Tittel, Hugo Zbinden, and Nicolas Gisin. "Long-distance teleportation of qubits at telecommunication wavelengths." In: Nature 421.6922 (2003), pp. 509–513.

[38] Hugues De Riedmatten, Ivan Marcikic, Wolfgang Tittel, Hugo Zbinden, Daniel Collins, and Nicolas Gisin. "Long distance quantum teleportation in a quantum relay configuration." In: Physical Review Letters 92.4 (2004), p. 047904.

[39] Hiroki Takesue, Shellee D. Dyer, Martin J. Stevens, Varun Verma, Richard P. Mirin, and Sae Woo Nam. "Quantum teleportation over 100 km of fiber using highly efficient superconducting nanowire single-photon detectors." In: Optica 2.10 (2015), pp. 832–835.

[40] Olivier Landry, Jeroen Anton Willem van Houwelingen, Alexios Beveratos, Hugo Zbinden, and Nicolas Gisin. "Quantum teleportation over the Swisscom telecommunication network." In: Journal of the Optical Society of America (JOSA) B 24.2 (2007), pp. 398–403.

[41] Matthäus Halder, Alexios Beveratos, Nicolas Gisin, Valerio Scarani, Christoph Simon, and Hugo Zbinden. "Entangling independent photons by time measurement." In: Nature physics 3.10 (2007), pp. 692–695.

[42] Félix Bussières, Christoph Clausen, Alexey Tiranov, et al. "Quantum teleportation from a telecom-wavelength photon to a solid-state quantum memory." In: Nature Photonics 8.10 (Oct. 2014), pp. 775–778. ISSN: 1749-4893. DOI: `10.1038/nphoton.2014.215`. URL: `https://doi.org/10.1038/nphoton.2014.215`.

[43] Ping Gao and Daniel Louis Jafferis. "A traversable wormhole teleportation protocol in the SYK model." In: Journal of High Energy Physics 2021.7 (2021), pp. 1–44.

[44] Evan Miyazono, Tian Zhong, Ioana Craiciu, Jonathan M Kindem, and Andrei Faraon. "Coupling of erbium dopants to yttrium orthosilicate photonic crystal cavities for on-chip optical quantum memories." In: Applied Physics Letters 108.1 (2016), p. 011111.

[45] Björn Lauritzen, Jiří Minář, Hugues De Riedmatten, Mikael Afzelius, Nicolas Sangouard, Christoph Simon, and Nicolas Gisin. "Telecommunication-wavelength solid-state memory at the single photon level." In: Physical Review Letters 104.8 (2010), p. 080502.

[46] Sacha Welinski, Philip J. T. Woodburn, Nikolai Lauk, Rufus L. Cone, Christoph Simon, Philippe Goldner, and Charles W. Thiel. "Electron Spin Coherence in Optically Excited States of Rare-Earth Ions for Microwave to Optical Quantum Transducers." In: Physical Review Letters 122 (24 June 2019), p. 247401. DOI: `10.1103/PhysRevLett.122.247401`. URL: `https://link.aps.org/doi/10.1103/PhysRevLett.122.247401`.

[47] C. K. Hong, Z. Y. Ou, and L. Mandel. "Measurement of subpicosecond time intervals between two photons by interference." In: Physical Review Letters 59 (18 Nov. 1987), pp. 2044–2046. DOI: `10.1103/PhysRevLett.59.2044`. URL: `https://link.aps.org/doi/10.1103/PhysRevLett.59.2044`.

[48] Joseph B. Altepeter, Evan R. Jeffrey, and Paul G. Kwiat. "Photonic state tomography." In: Advances in Atomic, Molecular, and Optical Physics 52 (2005), pp. 105–159.

[49] Xiongfeng Ma, Bing Qi, Yi Zhao, and Hoi-Kwong Lo. "Practical decoy state for quantum key distribution." In: Physical Review A 72.1 (2005), p. 012326.

[50] George Iskander, Neil Sinclair, Cristián Peña, Si Xie, and Maria Spiropulu. "Stabilization of an electro-optic modulator for quantum communication using a low-cost microcontroller." In: Caltech Undergraduate Research Journal 20.1 (2019).

[51] J. G. Rarity. “Interference of Single Photons from Separate Sources a.” In: Annals of the New York academy of Sciences 755.1 (1995), pp. 624–631.

[52] F. Marsili, V. B. Verma, J. A. Stern, et al. “Detecting single infrared photons with 93% system efficiency.” In: Nature Photonics 7.3 (Mar. 2013), pp. 210–214. ISSN: 1749-4893. DOI: `10.1038/nphoton.2013.13`. URL: `https://doi.org/10.1038/nphoton.2013.13`.

[53] Photon Spot. `https://www.photonspot.com/`. URL: `https://www.photonspot.com/`.

[54] N. Lütkenhaus, J. Calsamiglia, and K-A Suominen. “Bell measurements for teleportation.” In: Physical Review A 59.5 (1999), p. 3295.

[55] Ivan Marcikic, Hugues de Riedmatten, Wolfgang Tittel, Valerio Scarani, Hugo Zbinden, and Nicolas Gisin. “Time-bin entangled qubits for quantum communication created by femtosecond pulses.” In: Physical Review A 66.6 (2002), p. 062308.

[56] Leonard Mandel and Emil Wolf. Optical coherence and quantum optics. Cambridge university press, 1995.

[57] Tian Zhong and Franco NC Wong. “Nonlocal cancellation of dispersion in Franson interferometry.” In: Physical Review A 88.2 (2013), p. 020103.

[58] Reinhard F. Werner. “Quantum states with Einstein-Podolsky-Rosen correlations admitting a hidden-variable model.” In: Physical Review A 40.8 (1989), p. 4277.

[59] John F. Clauser, Michael A. Horne, Abner Shimony, and Richard A. Holt. “Proposed experiment to test local hidden-variable theories.” In: Physical Review Letters 23.15 (1969), p. 880.

[60] Hiroki Takesue. “1.5 μ m band Hong-Ou-Mandel experiment using photon pairs generated in two independent dispersion shifted fibers.” In: Applied physics letters 90.20 (2007), p. 204101.

[61] S. Massar and S. Popescu. “Optimal Extraction of Information from Finite Quantum Ensembles.” In: Physical Review Letters 74 (8 Feb. 1995), pp. 1259–1263. DOI: `10.1103/PhysRevLett.74.1259`. URL: `https://link.aps.org/doi/10.1103/PhysRevLett.74.1259`.

[62] Holger P Specht, Christian Nölleke, Andreas Reiserer, Manuel Uphoff, Eden Figueroa, Stephan Ritter, and Gerhard Rempe. “A single-atom quantum memory.” In: Nature 473.7346 (2011), pp. 190–193.

[63] Neil Sinclair, Erhan Saglamyurek, Hassan Mallahzadeh, et al. “Spectral Multiplexing for Scalable Quantum Photonics using an Atomic Frequency Comb Quantum Memory and Feed-Forward Control.” In: Physical Review Letters 113 (5 July 2014), p. 053603. DOI: `10.1103/PhysRevLett.113.053603`. URL: `https://link.aps.org/doi/10.1103/PhysRevLett.113.053603`.

[64] Dagmar Bruss, Artur Ekert, and Chiara Macchiavello. “Optimal universal quantum cloning and state estimation.” In: Physical Review Letters 81.12 (1998), p. 2598.

[65] Vladimir Bužek and Mark Hillery. “Quantum copying: Beyond the no-cloning theorem.” In: Physical Review A 54.3 (1996), p. 1844.

[66] Masahiro Takeoka, Rui-Bo Jin, and Masahide Sasaki. “Full analysis of multi-photon pair effects in spontaneous parametric down conversion based photonic quantum information processing.” In: New Journal of Physics 17.4 (Apr. 2015), p. 043030. DOI: `10.1088/1367-2630/17/4/043030`. URL: `http://dx.doi.org/10.1088/1367-2630/17/4/043030`.

[67] Christian Weedbrook, Stefano Pirandola, Raúl García-Patrón, Nicolas J. Cerf, Timothy C. Ralph, Jeffrey H. Shapiro, and Seth Lloyd. “Gaussian quantum information.” In: Rev. Mod. Phys. 84 (2 May 2012), pp. 621–669. DOI: `10.1103/RevModPhys.84.621`. URL: `https://link.aps.org/doi/10.1103/RevModPhys.84.621`.

[68] Di Zhu, Marco Colangelo, Changchen Chen, Boris A Korzh, Franco NC Wong, Matthew D Shaw, and Karl K Berggren. “Resolving Photon Numbers Using a Superconducting Nanowire with Impedance-Matching Taper.” In: Nano Letters 20.5 (2020), pp. 3858–3863.

[69] Hari Krovi, Saikat Guha, Zachary Dutton, Joshua A Slater, Christoph Simon, and Wolfgang Tittel. “Practical quantum repeaters with parametric down-conversion sources.” In: Applied Physics B 122.3 (2016), p. 52.

[70] P. J. Mosley, J. S. Lundeen, B. J. Smith, P. Wasylczyk, A. B. U’Ren, C. Silberhorn, and I. A. Walmsley. “Heralded Generation of Ultrafast Single Photons in Pure Quantum States.” In: Physical Review Letters 100.13 (2008). Demonstrates spectral engineering for single–mode operation and reports high heralding efficiency and purity (as indicated by low $g^{(2)}(0)$)., p. 133601.

[71] R. Maleck Rassoul, A. Ivanov, E. Freysz, A. Ducasse, and F. Hache. “Second-harmonic generation under phase-velocity and group-velocity mismatch: influence of cascading self-phase and cross-phase modulation.” In: Optics Letters 22.5 (1997), pp. 268–270.

[72] Boris Korzh, Qing-Yuan Zhao, Jason P Allmaras, Simone Frasca, Travis M Autry, Eric A Bersin, Andrew D Beyer, Ryan M Briggs, Bruce Bumble, Marco Colangelo, et al. “Demonstration of sub-3 ps temporal resolution with a superconducting nanowire single-photon detector.” In: Nature Photonics 14.4 (2020), pp. 250–255.

[73] R. Valivarthi, I. Lucio-Martinez, A. Rubenok, et al. In: Optics Express 22.20 (2014), pp. 24497–24506.

[74] Raju Valivarthi, Qiang Zhou, Caleb John, Francesco Marsili, Varun B Verma, Matthew D Shaw, Sae Woo Nam, Daniel Oblak, and Wolfgang Tittel. “A cost-effective measurement-device-independent quantum key distribution system for quantum networks.” In: Quantum Science and Technology 2.4 (2017), 04LT01.

[75] Qi-Chao Sun, Ya-Li Mao, Yang-Fan Jiang, et al. “Entanglement swapping with independent sources over an optical-fiber network.” In: Phys. Rev. A 95 (3 Mar. 2017), p. 032306. DOI: `10.1103/PhysRevA.95.032306`. URL: `https://link.aps.org/doi/10.1103/PhysRevA.95.032306`.

[76] Samuel L Braunstein and Stefano Pirandola. “Side-channel-free quantum key distribution.” In: Physical Review Letters 108.13 (2012), p. 130502.

[77] Daniel Gottesman and Isaac L. Chuang. “Demonstrating the viability of universal quantum computation using teleportation and single-qubit operations.” In: Nature 402.6760 (1999), pp. 390–393.